Soft Matter

PAPER

Check for updates

Effect of polymer–nanoparticle interaction on strain localization in polymer nanopillars†

Entao Yang, [ID] [a] Robert J. S. Ivancic, [ID] [b] Emily Y. Lin [ID] [a] and Robert A. Riggleman [ID] *[a]

Polymer nanocomposites (PNCs), a class of composites consisting of typically inorganic nanoparticles (NPs) embedded in a polymer matrix, have become an emerging class of materials due to their significant potential to combine the functionality of NPs with the toughness of polymers. However, many applications are limited by their mechanical properties, and a fundamental understanding of NPs' effect on the nonlinear mechanical properties is lacking. In this study, we used molecular dynamics simulations to investigate the influence of NPs on the tendency of a polymer nanopillar to form a shear band. Even though we restrict ourselves to sufficiently low NP loadings that the elastic and yield behaviors are unaffected compared to the pure polymer, the polymer–NP interactions have a surprisingly strong effect on the location of a shear band in the sample. Different polymer–NP interactions have been used to explore their effect on the local structure of materials which is described using a recently developed machine-learned quantity, softness. Our calculations reveal a strong correlation between the strain localization pattern and the local structural signatures. Lastly, we show that weak interactions between NP and polymer matrix can form a soft region near the NP, and this leads to an attraction of the shear band to the NP surface.

Introduction

Polymer nanocomposites (PNCs) typically consist of a polymer matrix loaded with inorganic nanoparticles (NPs). Due to the high surface-to-volume ratio, the NPs can dramatically enhanced materials' electrical, thermal, and mechanical properties, even at a low concentration.[1–3] As a result, PNCs have been used in a wide range of fields, ranging from electronics[4] to gas separation process.[5] However, many applications can be limited due to the brittle nature of PNCs, which can lead to catastrophic failure.[6] There are many studies that have examined the effects of different factors on PNCs' mechanical properties, such as NP size,[7] mobility,[8] dispersion state,[9] and grafting,[7,10] but the inherent connection between polymer–NP interactions and their influence on the local structure and the consequences for material failure are not well understood. Since isolating effects of NP size, dispersion state, and NP surface roughness is experimentally challenging, simulation becomes an effective method to facilitate a fundamental understanding of the physics underlying mechanical properties of PNCs.

Polymer–NP interactions play a critical role in PNCs' mechanical properties. Adding attractive or neutral NPs can increase the average shear and Young's modulus, alter polymers' nonaffine displacement field during the deformation, and render the material less fragile.[11,12] The primary mechanism of this reinforcement is the presence of an interfacial polymer layer around NPs, where polymers have a different segmental packing and a modified mobility.[11,13,14] Quantities like the layer width, the interfacial polymer density, and the interfacial dynamics are strongly dependent on polymer–NP interactions.[15] A slow dynamical layer near NPs with an attractive polymer interaction can have the relaxation time increased by several orders of magnitude compared with the bulk polymer; this finding has been observed in both experiments[16–18] and simulation.[13,19–21] In contrast, for weaker or repulsive polymer–NP interactions, the near-surface dynamics are typically accelerated.[15,22,23]

Strain localization in amorphous solids, commonly referred to as shear banding, occurs when large shear strains localize into a relatively thin band. It has been observed experimentally in many amorphous materials, including granular materials,[24] amorphous alloys,[25,26] and metallic glasses,[27,28] and it is widely accepted that the strain localization leads to the failure of amorphous solids.[29–32] The formation of shear band can be

a Department of Chemical and Biomolecular Engineering, University of Pennsylvania, Philadelphia, PA 19104, USA. E-mail: rrig@seas.upenn.edu
b Department of Physics and Astronomy, University of Pennsylvania, Philadelphia, PA 19104, USA
† Electronic supplementary information (ESI) available: Attached. See DOI: 10.1039/d0sm00991a

affected by many factors, including strain rates, temperature, and sample preparation.[33,34] Although there is no obvious structural difference between the strain localization region and the others, previous work shown that shear band location depends on the structural features that are frozen during sample preparation,[35,36] implying a strong correlation between the shear band location and the local structures of particles.

Recently, a novel machine learning application has been proposed which uses the Support Vector Machine (SVM) algorithm to identify particles that tend to rearrange in a short time window based on the instantaneous local structure.[37,38] A new scalar quantity 'softness' has been defined[39] to indicate the relative probability of a particle to exhibit a rearrangement.[38] This quantity has expanded our understanding of glassy liquds[39,40] and aging in glassy materials.[41] In particular, it has been critical in the understanding of the universal yield strain of glassy materials[38] and the determination of shear band initiation from a microscopic perspective.[36]

In this work, we generate a family of nanopillars with a single NP embedded in their center and probe the effect of polymer–NP interactions on strain localization in the pillar. Using a single NP can be an efficient approach in simulation studies of PNCs,[15,42,43] because it helps isolate the effect of interactions between polymer and NP on the resulting mechanical response from the dispersion and overall distribution of the NPs, which are inherently coupled in multi-particle simulations. Surprisingly, we find that although the elastic and yield properties are unaffected, the location of shear bands can be controlled by the nanoparticles. We characterize the local structure around NP surfaces using softness and find that weak polymer–NP interactions lead to soft regions near the particle surfaces. We also find that weak polymer–NP interactions tend to attract shear bands to the region near NP surface, while stronger polymer–NP interactions lead to a region less prone to shear banding. During the deformation, we find a region near NP surfaces with a gradient in the strain rate, and we qualitatively compare the size of this region to the region with a disrupted structure. The size of NPs has also been varied to quantify their effects on local structure and dynamics.

Method

System initialization

We used a coarse-grained bead-spring model to construct the polymer matrix in our simulations.[44] Polymer chains consist of 10 Lennard-Jones (LJ) interaction sites representing the monomers, which are connected by harmonic bonds. All the systems have 2200 chains, yielding a total of 22 000 polymer particles. The standard 12-6 Lennard-Jones cut-and-shifted potential is used to describe all the non-bonded interactions,

$$U^{nb}(r_{ij}) = 4\varepsilon_{ij}\left[\left(\frac{\sigma}{r_{ij}}\right)^{12} - \left(\frac{\sigma}{r_{ij}}\right)^{6}\right] - U_{cut}, r_{ij} < 2.5\sigma$$

where U_{cut} is the value of the 12-6 potential at our cut-off distance, $r_c = 2.5\sigma$. Both polymer–polymer (ε_{pp}), and NP–NP

(ε_{nn}) interactions are fixed at 1.0, while the polymer–NP (ε_{pn}) interaction is varied from 0.2 to 3.0. The bonded interactions are described by the harmonic bonding potential,

$$U_{ij}^{b} = K(r - \sigma)^2$$

where $K = 400\varepsilon/\sigma^2$, and σ is the diameter of monomers. All the units reported in this paper are in LJ reduced units. The reduced temperature, T, is expressed as $T = kT^*/\varepsilon$, and the LJ time, $\tau_{LJ} = t^*\sqrt{\varepsilon/m\sigma^2}$, where k is the Boltzmann constant, m is the mass of a single LJ interaction site, T^* is temperature, and t^* is time and the asterisk indicates quantities in laboratory units.

The NP is modelled as an amorphous and rigid sphere of LJ sites, with a nominal radius of $R_p = 3.0$, 4.0 or 5.0σ. To construct the amorphous NP, we first equilibrated a bulk LJ liquid at high temperature ($T = 10.0$) and high density ($\rho_0 = 1.25$). We then cut a spherical solid from the LJ fluid by selecting all of the particles within R_p of a point in the fluid. Particles that are outside of the sphere were deleted. The resulting NP configuration has the same density as the high temperature, high pressure LJ liquid, thus ensuring the amorphous nature of the NP. We constructed one NP for each radius, guarantying the same surface roughness as a function of ε_{pn} for the same size of NPs. Also due to its amorphous nature, the actual radius could be slightly smaller than the nominal radius in some part of the NP. For simplicity, we used the nominal radius as the position of NP surface in this work and distance between NP surface and polymer monomers can be slightly negative in some cases.

We believe the rigid NP approximation employed here is reasonable, because NPs are frequently much stiffer than polymer matrix. We also note that previous work has shown that in supported polymer films, the stiffness of the substrate will not qualitatively change polymer dynamical profiles, especially for thick films.[45] Our softness analysis presented later also proves that the polymer packing change due to stiffness is much smaller compared with the polymer–NP interactions. Thus, we do not expect to see any qualitative change in our results without this approximation.

To build the PNC pillars, we first place the NP at the center of a simulation box, and fill the simulation box with polymer chains surrounding the NP, then we confine the system to a pillar geometry, where the height (H) and diameter (D) are 50σ, and 25σ, respectively. Polymer chains are inserted into the cylinder space on a mesh with 1σ resolution initially, surrounding the NP. Periodic boundary conditions are used along the lengths of the pillar (z-direction), and the pillar geometry is initially maintained by using a harmonic repulsive wall in the radial direction, which is 14.0σ away from the pillar center. Pure polymer pillars with a same number of polymer chains were also constructed as a control group following a similar protocol.

All the systems were first equilibrated in the *NVT* ensemble at $T = 1.0$ until the polymers had diffused many times their end-to-end distance. The confining wall was then removed to construct a pillar with free surfaces, and the systems were
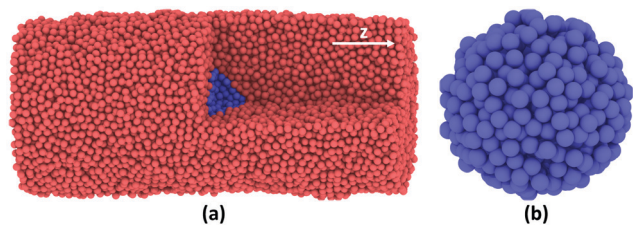
Fig. 1 (a) Visualization of our cylindrical PNC system. The pillar is cut to display the nanoparticle (colored in blue) in the center. (b) Image of rigid amorphous nanoparticle, $R_p = 5.0\sigma$. These snapshots were created using OVITO software.[52]

further equilibrated at $T = 1.0$. Equilibration proceeded until the polymers had diffused farther than their equilibrium end-to-end distance. Independent configurations were generated at this high temperature and were separated by approximately a diffusion time. A typical snapshot of the system and the amorphous NP are shown in Fig. 1.

Following the equilibration, all the systems were quenching to $T = 0.1$, which is much less than the glass transition temperature T_g (~ 0.43), with a constant rate $\Gamma = 5 \times 10^{-4}\tau_{LJ}^{-1}$. T_g was determined by monitoring the density during the quenching process. Linear fits were performed above and below the transition region, and the corresponding temperature of the intersection point between these two lines was taken as the glass transition temperature. In most of the work presented below, unless specified, we use the system with NP radius equals to 5.0σ. All the simulations were performed using the LAMMPS package[46] with a timestep $\delta t = 0.002\tau_{LJ}$, and all results are averaged over 3 to 20 independent configurations.

Pillar deformation and strain localization

To study the mechanical properties of these PNC pillars, we applied uniaxial tension along the length of the pillars with a constant true strain rate $\dot{\varepsilon} = 10^{-4}$. During deformation, the system stress and particle positions were stored at a fixed interval. To measure the degree of strain localization, we calculated the local deviatoric strain rate, J_2, using a previously established method.[47] The equation for J_2 is:

$$J_2(i, t, \Delta t) = \frac{1}{\Delta t}\sqrt{\frac{1}{3}\mathrm{Tr}\left[\frac{1}{3}(\boldsymbol{J}_i^T\boldsymbol{J}_i - \boldsymbol{I}) - \frac{1}{3}\mathrm{Tr}(\boldsymbol{J}_i^T\boldsymbol{J}_i - \boldsymbol{I})\right]^2}$$

where $\boldsymbol{J}_i$ is the best-fit local affine transformation matrix for particle i after small strain (Δt), which can be calculated from particle and its neighbours' positions.[30] Particle neighborhood is defined with a cut off radius of 2.5σ, which is the same as LJ interaction length. A particle with a large J_2 value indicates that the particle has a high shear strain rate.

Softness and P_{hop} calculations

To calculate the softness of polymer monomers, we used a similar scheme as described in ref. 36–40. The basic idea is to employ a large group of structure functions to distinguish the local structures of particles that have a tendency to rearrange from those that tend to not rearrange for a prolonged period. A

training set of rearranging and non-rearranging particles is generated, and each particle is characterized by the set of structure functions, which form a vector in a high-dimensional space with dimensionality equal to the total number of structure functions. We then employ a support vector machine (SVM) algorithm to identify the hyperplane that best separates the rearranged and the non-rearranged particles, which are labelled as soft and hard particles respectively. The softness of a given particle is defined as the signed distance between the hyperplane and its corresponding point in the high dimensional space, which is positive on the soft (likely to rearrange) side and negative on the other.

In this work, we define two groups of structure functions for each particle i:

$$G_R(i; \mu, L) = \sum_j \max(e^{-(R_{ij} - \mu)^2/L^2} - \varepsilon_R, 0)$$

$$G_A(i; \xi, \lambda, \zeta) = \sum_j \sum_k \max\left(e^{-(R_{ij}^2 + R_{ik}^2 + R_{jk}^2)/\xi^2}\left(\frac{1 + \lambda\cos\theta_{ijk}}{2}\right)^\zeta - \varepsilon_A, 0\right)$$

where R_{ij} is the distance between particle i and particle j; θ_{ijk} is the angle between particle i, j, and k; μ, L, ξ, λ, ζ are all parameters varied to construct different structure functions. The G_R group of structure functions describe the local radial structure characteristics of each particle. It can also be regarded as a Gaussian-smoothed version of the radial distribution function, $g(r)$, for the particle i. The G_A group of structure functions contain the bond orientation information among the three particles.

In contrast to previous approaches which have an explicit built-in cut-off radius, we determine the cut-off radius of these structure functions implicitly by parameters $\varepsilon_R, \varepsilon_A \in (0,1)$. This ensures that these structure functions are smooth at the determined cut-off radius. Larger values of ε_R and ε_A simply correspond to a larger discontinuity in derivatives of these functions at the cut off radius. We have found that our results are insensitive to this so long as they are chosen reasonably small. Here, we choose $\varepsilon_R = 0.01$ and $\varepsilon_A = 0.05$. The cutoff distance, R_{cut}, is approximately 2.5σ. More details about R_{cut} determination can be found in the ESI.†

In this work, given that we have a relatively simple model system with only one monomer size, we used 30 radial structure functions and 10 angular structure functions. These parameters can be found in the ESI.† Thus, the total dimensions of the structure functions are $M = 40$. Then we assign the structure functions of each monomer i to a vector $\vec{p}_i \in {}^{40}\mathbb{R}$. The elements in this feature vector serve as the coordinates of each particle's corresponding point in the 40-dimensional space.

The next step in computing a softness field is constructing a "training set", a set of particles about to rearrange and a set that have not rearranged for a long time. Though this has been done in mechanically deformed systems below the glass transition,[36,37,41,48] it is significantly more difficult than in quiescent systems as one must worry about obtaining enough rearrangements for training, what constitutes a monomer being non-rearranging for a "long time" in a mechanically

deformed system, and how strain localization affects results. Instead, we have collected our training data from a pure polymer system above T_g in the *NPT* ensemble at $T = 0.5$ and $P = 0$, since it has been shown that the softness field is invariant to changes in temperature.[39] In this simulation, we collect 10 000 configurations with an output frequency of $t_f = 0.1\tau_{LJ}$.

We use P_{hop} as the indicator of particles' local rearrangements, which is introduced by Candelier *et al.*[49,50] P_{hop} is defined as:

$$P_{hop}(t) = \sqrt{\langle (r_i - \langle r_i \rangle_B)^2 \rangle_A \langle (r_i - \langle r_i \rangle_A)^2 \rangle_B}$$

which is calculated at time t by first defining a lag time t_R and two time intervals $A = [t - t_R/2, t]$, and $B = [t, t + t_R/2]$. r_i represents the position of particle i at an instant in the time interval. And the $\langle \rangle_A$, $\langle \rangle_B$ represent the average over different time intervals. Based on previous work[51] and our own optimizations, we define a rearranging particle if its P_{hop} value is great than 0.25. The non-rearranging particle is defined if its P_{hop} value remains below 0.05 for 200 frames, corresponding to a time interval of $20\tau_{LJ}$.

To construct our training set, 20 000 rearranging particles (labelled as 'soft') and an equal number of non-rearranging particles (labelled as 'hard') are chosen randomly from our quiescent simulation. We then use a linear Support Vector Machine (SVM) to find a hyperplane that best separates the soft and the hard particles in the high dimensional space defined by our set of structure functions. The normal to this hyperplane is the output of our training and can be used to calculate the softness, and the projection of a particle's position in this hyperspace onto the normal provides a signed "distance" to the hyperplane, which we take as the particle's softness. This hyperplane trained on the neat polymer is then used for all our PNC systems at all temperatures. We find that the fraction of rearranged particles labelled as soft is above 93% in all six interactions, indicating we only mislabel 7% of the rearrangements. The overall percentage of correctly classified particles, including both the rearranged and the non-rearranged particles, ranges from 92% to 97%.

Results

Macroscopic mechanical properties and dynamics of the deforming process

We began our analysis by characterizing the mechanical properties of these polymer nanopillars, using 20 independent configurations for each ε_{pn}. The average true stress–strain curves of different systems during the deformation are plotted in Fig. 2. We find that the elastic modulus, yield stress, and yield strain are essentially unaffected by changes in ε_{pn}. This is not unexpected given that we only have one NP in the center of the nanopillar, giving a NP volume fraction of less than 3%. As our main focus in this study is on the effect of polymer–NP interactions on nanopillars' failure mode and shear band location, the lack of a change in the stress–strain curve is unimportant for our primary conclusions.
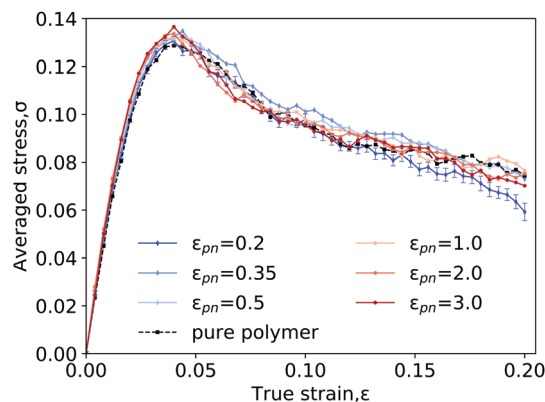

Fig. 2 Stress–strain curves of pure polymer pillar and polymer nanopillars with different polymer–NP interactions. Error bars for different systems are in a similar magnitude and is only shown for the dark blue curve ($\varepsilon_{pn} = 0.2$).

We next calculated particles' deviatoric strain rate, J_2, during the deformation. In Fig. 3, we plot the average J_2, $\langle J_2 \rangle$, around the NP as a function of the radial distance from NP surface for systems with different ε_{pn} at 2 different strains, $\lambda = 0.2\%$ and $\lambda = 3.4\%$. Results of pure polymer pillars are presented as well, and the distance is calculated as the distance to pillar center, minus the NP's nominal radius, $R_p = 5.0\sigma$. The lag strain for the J_2 calculation is 0.4%, corresponding to a time interval of $t = 40\tau_{LJ}$, and $\langle J_2 \rangle$ is averaged over 20 configurations. Fig. 3 shows that at
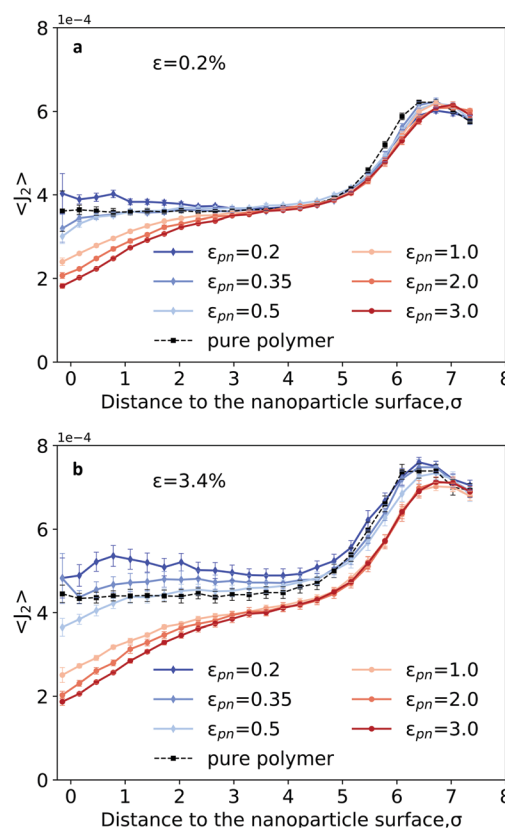

Fig. 3 Average J_2 values ($\langle J_2 \rangle$) as a function of distance to the nanoparticle surface in the radial direction. (a) strain $\lambda = 0.2\%$; (b) strain $\lambda = 3.4\%$.

each strain, $\langle J_2 \rangle$ as a function of distance from NP surface can be roughly divided into three regions. In the first region, which is immediately adjacent to NP surface (0 to 2.5σ), effect of ε_{pn} dominates changes in $\langle J_2 \rangle$. In systems with smaller ε_{pn}, $\langle J_2 \rangle$ value is higher, which indicates that these particles rearrange more easily. As ε_{pn} increases, the plasticity measured by $\langle J_2 \rangle$ decreases. Following the near-NP region, particles behave more bulk-like; $\langle J_2 \rangle$ is stable, and it is relatively unaffected by changes in polymer–NP interactions. The last region contains particles near free surface, and the higher mobility near the free surface leads to a sharp increase in $\langle J_2 \rangle$. The peak we saw in Fig. 3 locates near the pillar surface, since our pillars have a radius around 12.5σ and NP radius is 5.0σ.

Fig. 3 also shows that differences in $\langle J_2 \rangle$ among systems with different polymer–NP interactions increase as strain increases, and above a threshold strain, the systems with weaker ε_{pn} ($\varepsilon_{pn} = 0.2, 0.35$) have a higher J_2 at all distances from NP surface. This result indicates that adding a weakly interacting NP can drastically increase particles' local deviatoric strain rate throughout the entire pillar radially. We will show below that this is due to the tendency of shear bands to form near NPs with weaker interactions. We can also see that a weak interaction $\varepsilon_{pn} = 0.5$, but not the neutral interaction ($\varepsilon_{pn} = \varepsilon_{pp} = 1.0$), is more like the intermediate state. This is expected since NP itself can alter polymers packing and slow down dynamics around it.

Calculating J_2 using longer lag strains of 5.6% and 8.0% allows us to easily identify the location of the shear band in the vicinity of the yield point. Fig. 4a and b show the position of the shear band in two cases, one where the shear band forms near the NP (Fig. 4a) and one far from the NP (Fig. 4b). These two snapshots were cut from pillars with $\varepsilon_{pn} = 0.2$ and $\varepsilon_{pn} = 3.0$ respectively. We also noticed that these interactions are not the prerequisites for the shear banding positions. In another word, shear bands can form away from NP when $\varepsilon_{pn} = 0.2$, and near NP when $\varepsilon_{pn} = 3.0$, but with different probabilities.

Thus, to further quantify the distance between the shear band and the NP, we divided our pillars into $N_{plane} = 900$ planes uniformly, with 25 bins in the $\hat{z}$ axis and 36 bins in the $\hat{\theta}$ direction. All the planes have a same polar angle of $45°$, considering shear bands are expected to form along approximately $45°$ in the pillars. Thus, each plane is 2σ wide in the z direction, corresponding to a real width of 1.41σ. We then average J_2 over each plane $\langle J_2 \rangle_p$, with the longer lag strains calculated in each plane, and take the plane with the largest $\langle J_2 \rangle_p$ as the shear band plane. According to our measurements, the average $\langle J_2 \rangle_p$ for the shear banding plane in different pillars is $\langle J_2 \rangle_p = 2.5 \times 10^{-4} \tau_{LJ}^{-1}$, while for the typical non-shear plane (the farthest parallel plane of the shear banding plane) is $\langle J_2 \rangle_p = 7.2 \times 10^{-5} \tau_{LJ}^{-1}$. Both values have a stand error in the order of $10^{-6} \tau_{LJ}^{-1}$. This large difference (a factor of 3.5) further proves the existence of strain localization in our pillars.

Next, we calculated the normal distance between NP center and the shear band plane and plot it as a function of polymer–NP interactions around and post yield (Fig. 4c). When the interactions are weaker ($\varepsilon_{pn} = 0.2, 0.35$), shear bands tend to form near NP. When the interactions become more attractive,
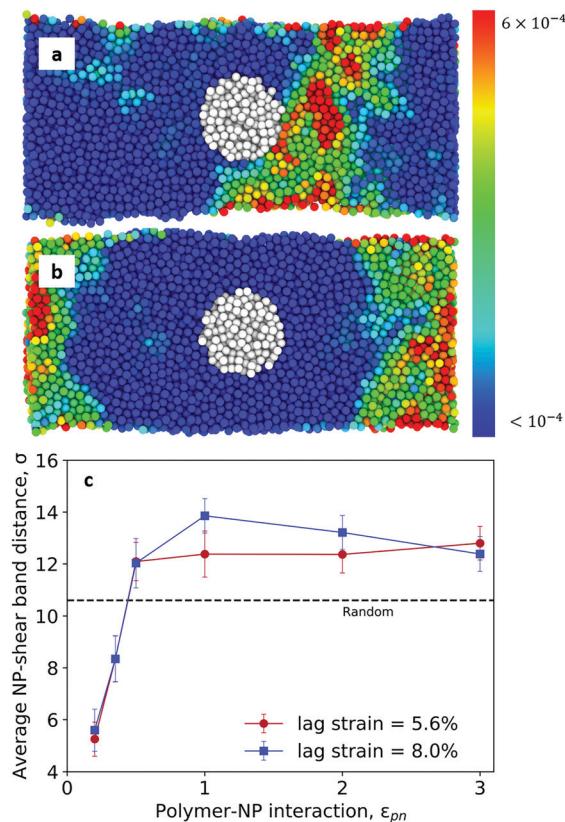

Fig. 4 Visualization of the pillars with shear band, formed around yield. Particles are colored based on J_2 values. (a) shear band formed near nanoparticle, picked from the weakest interaction, $\varepsilon_{pn} = 0.2$. (b) shear band formed away from nanoparticle, picked from the strongest interaction, $\varepsilon_{pn} = 3.0$. (c) Averaged nanoparticle-shear band distance at different lag strains: the dash line represents the average distance between nanoparticle center and randomly distributed shear bands between particle surface and edge of simulation box along the pillar length. The visualization of pillars were created using OVITO software.[52]

shear bands are less likely to form near NP and is distributed in regions far from NP. This general trend is insensitive to the lag strain we used to calculate $\langle J_2 \rangle$. The randomly distributed shear bands (between particle surface and edge of simulation box along the pillar length) is also given as a reference. This is different from the average distance between pillar center and shear band in pure polymer pillars, which is around 8.6σ, because shear bands are unlikely to form across the NP, and all the pillars have a same dimension.

To quantitatively illustrate the shear band location as a function of polymer–NP interactions, we calculated a Gaussian-smeared probability density distribution of distance to the shear band, d,

$$P(d) = \frac{1}{NL\sqrt{2\pi}} \sum_{i=1}^{N=20} e^{-(R_i-d)^2/2L^2},$$

where R_i is the distance between the NP and the shear band plane, L is constant distribution bin size, d is the position at the center of each bin, representing different distance to the NP center. The only purpose of the normalization here is to get more smooth
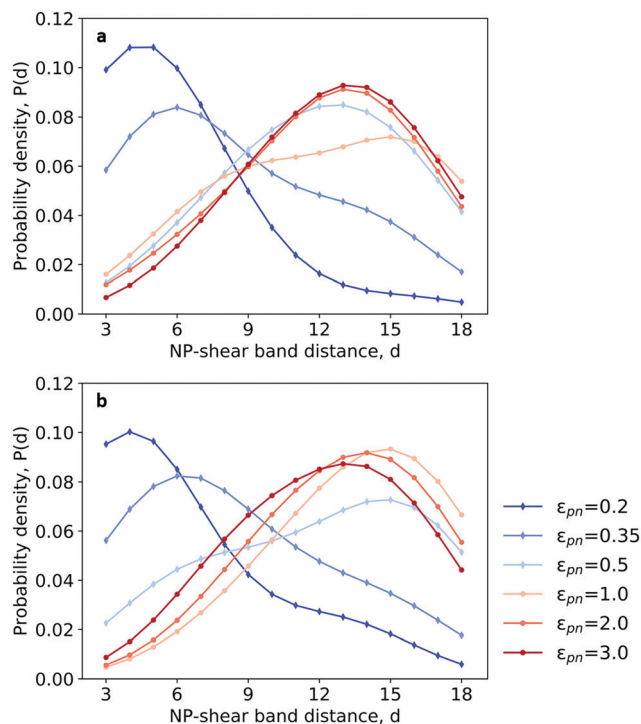
Fig. 5 Probability density distribution of NP-shear band distance at different lag strains: (a) lag strain = 5.6%; (b) lag strain = 8.0%.
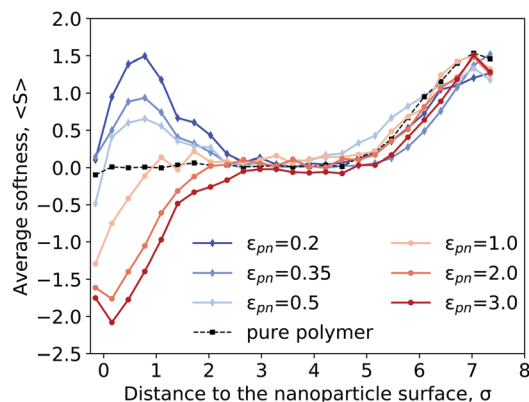

Fig. 6 Average softness values as a function of distance to the nano-particle surface in polymer nanopillars with nanoparticle radius $R_p = 5.0\sigma$.

curves. In Fig. 5, we calculated $P(d)$ with $L = 1\sigma$, for all six polymer–NP interactions using two different lag strains (5.6% and 8.0%). Systems with weaker polymer–NP interactions ($\varepsilon_{pn} = 0.2, 0.35$) tend to form shear bands near the NP. Distance from the NP quickly saturates as ε_{pn} increases, and the distribution becomes essentially constant. This is consistent with our previous results in deviatoric strain rate distribution, J_2, in Fig. 3, where $\varepsilon_{pn} = 0.5$ is more like an intermediate state between weak and strong interactions.

Local structure and dynamics above T_g

We next characterized the softness near NPs at a temperature above T_g ($T = 0.5$) using the hyperplane trained from a bulk polymer liquid. Due to our choice of using an amorphous NP that consists of Lennard-Jones sites, we include the NP sites in the characterization of structure around polymer monomers near NP surface. This eliminates the presence of an artificial void in the local neighborhood of particles adjacent to NP surface, which would result in unphysically large softness. In the ESI,† we provide numerical justification for this approximation by showing that the softness curves are unaltered when changing the cut-off used in softness calculation, which provides evidence that the softness changes observed are due to changes in the local structure of the polymer monomers and not the inclusion of NP interaction sites. In Fig. 6, we plot average softness as a function of distance from NP surface in the radial direction for all six polymer–NP interactions and the pure polymer pillar. Three distinct regions of softness appear again, like the trend of J_2 shown in Fig. 3. In the near-NP region, the average softness decreases significantly with the increase of ε_{pn}.

It indicates that weaker interactions make polymers in the near-NP region 'softer' and more likely to rearrange, leading to higher probability of strain localization, as shown in Fig. 4 and 5. For distances just beyond the near-NP region, there is a bulk region where the averaged softness is approximately zero, indicating the effect of NP does not extend into this region. Like what was shown in Fig. 3, a free surface region is also observed in the softness distribution due to the reduction in neighbors for particles near nanopillar surface. This can be further verified by softness in pure polymer pillar, which fluctuates around zero and shows a sharp increase near surface.

In Fig. 7, we demonstrated that effect of NP size is relatively weak on softness of polymer monomers in the near-NP region. We calculated average softness as a function of distance to NP surface for three interaction strengths and NP sizes, $R_p = 3.0$, 4.0, and 5.0σ. Similar trends are observed for all NP sizes. The only significant effect of NP size on average softness is the enhanced separation of three regions in smaller NP systems, which can be seen visually as the horizontal shift of the same color curves. This is due to their being more distance between the particle surface and the nanopillar free surface, considering all pillars have a same dimension.
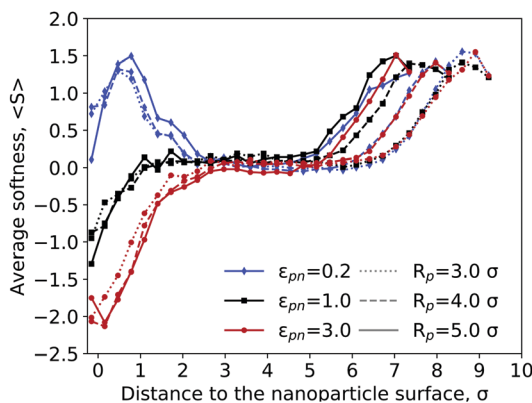

Fig. 7 Average softness as a function of distance to the nanoparticle surface for systems with different sizes of nanoparticles (denoted by different line styles) and polymer–NP interactions (denoted by different colors).
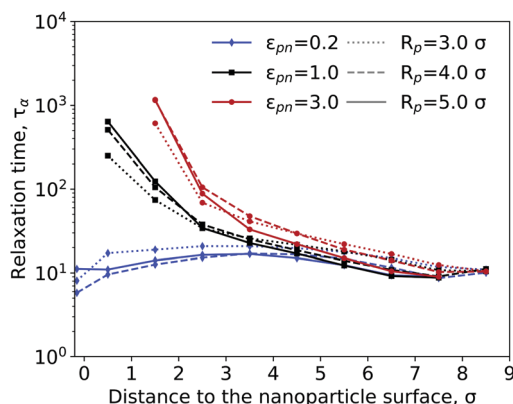
Fig. 8 Segmental relaxation time *vs.* distance to the nanoparticle surface. Different polymer–NP interactions are denoted by color. Different nanoparticle radius is denoted by line style.

Finally, we examined the average segmental relaxation time, τ_α, of the polymer as a function of distance to NP to further demonstrate the effect of polymer–NP interaction at different positions. Previous work has shown that segmental relaxation time can be robustly predicted using softness,[41] thus we expect to see a strong correlation between the relaxation time and the softness. Considering we have measured J_2 at a temperature below T_g, which represents polymer dynamics as well, it can be helpful if we have a measure of the relaxation time above T_g. We kept the polymer nanopillars at $T = 0.5$, at equilibrium above $T_g(\sim 0.43)$, to calculate segmental relaxation time from the intermediate scattering function, $F_s(q,t)$. This is also the same temperature we measured softness, so that we can better evaluate the correlations. τ_α is taken as the time when $F_s(q,t)$ decays to 0.2. In Fig. 8, we showed τ_α as a function of distance to NP surface. The segmental relaxation time is independent of ε_{pn} far from the NP, but a strong function of ε_{pn} near NP surface. For systems with strongly attractive polymer–NP interactions, relaxation time is significantly increased near NP. In other words, polymer monomers near NP surface are greatly restricted by the NP and cannot get relaxed in an accessible simulation time. This observation is consistent with our previous analyses, outlined in Fig. 3–7. The length scale of the recovery to the bulk relaxation time is larger than that of the softness (and J_2 distributions obtained below T_g), which is also consistent with previous results shown by Sussman, *et al.*,[51] where the ability of softness to predict mobility decrease near interfaces in polymer thin films.

Conclusions

We used molecular dynamics simulation to study the strain localization in polymer nanopillars under tensile deformation. Polymer nanopillars with varied polymer–NP interactions as well as NP sizes were constructed. We measured the macroscopic mechanical responses to deformation below T_g, and found the polymer–NP interaction does not significantly change the macroscopic stress–strain behavior at this NP loading; however,

the location of shear band formation was strongly affected by the polymer–NP interactions. We employed different metrics for quantifying microscopic structure and particle-level dynamics, we showed that by tuning the interactions between polymer and NP, one can control the location of the strain localization. Weaker polymer–NP interactions lead to a softer region around the NP, which ultimately leads to a higher probability of shear band formation. Thus, it is possible to control the shear band formation of a polymer pillar by adding NPs and varying the interactions. We note that in pure polymer nanopillars surface fluctuations also play an important role in shear banding even for nanopillars larger than those considered.[36] However, our results imply that weakly interacting NPs can attract the shear bands, despite the expected strong role of surface effects. The increased internal mobility around these weak NPs can overcome any effects of the surface defects and attract shear bands. The results of our study are encouraging because they illustrate a strong connection between the structural signature found above the glass transition temperature, T_g, and the strain localization below T_g, which further demonstrates that shear band position greatly depends on the structural features of materials.

Conflicts of interest

There are no conflicts to declare.

Acknowledgements

References

1 A. C. Balazs, T. Emrick and T. P. Russell, *Science*, 2006, **314**, 1107–1110.

2 B. T. McGrail, A. Sehirlioglu and E. Pentzer, *Angew. Chem., Int. Ed.*, 2015, **54**, 1710–1723.

3 A. J. Crosby and J. Y. Lee, *Polym. Rev.*, 2007, **47**, 217–229.

4 M. Tyagi and D. Tyagi, *Int. J. Electron. Electr. Eng.*, 2014, **7**, 603–608.

5 S. K. Kumar, B. C. Benicewicz, R. A. Vaia and K. I. Winey, *Macromolecules*, 2017, **50**, 714–731.

6 R. O. Ritchie, *Nat. Mater.*, 2011, **10**, 817–822.

7 H. Chao and R. A. Riggleman, *Polymer*, 2013, **54**, 5222–5229.

8 D. Shah, P. Maiti, D. D. Jiang, C. A. Batt and E. P. Giannelis, *Adv. Mater.*, 2005, **17**, 525–528.

9 J. Y. Lee, Q. Zhang, T. Emrick and A. J. Crosby, *Macromolecules*, 2006, **39**, 7392–7396.

10 J. F. Moll, P. Akcora, A. Rungta, S. Gong, R. H. Colby, B. C. Benicewicz and S. K. Kumar, *Macromolecules*, 2011, **44**, 7473–7477.

11 G. J. Papakonstantopoulos, K. Yoshimoto, M. Doxastakis, P. F. Nealey and J. J. De Pablo, *Phys. Rev. E: Stat., Nonlinear, Soft Matter Phys.*, 2005, **72**, 1–6.

12 G. J. Papakonstantopoulos, M. Doxastakis, P. F. Nealey, J. L. Barrat and J. J. De Pablo, *Phys. Rev. E: Stat., Nonlinear, Soft Matter Phys.*, 2007, **75**, 1–13.

13 F. W. Starr, T. B. Schrøder and S. C. Glotzer, *Macromolecules*, 2002, **35**, 4481–4492.

14 S. Cheng, V. Bocharova, A. Belianinov, S. Xiong, A. Kisliuk, S. Somnath, A. P. Holt, O. S. Ovchinnikova, S. Jesse, H. Martin, T. Etampawala, M. Dadmun and A. P. Sokolov, *Nano Lett.*, 2016, **16**, 3630–3637.

15 W. Zhang, H. Emamy, B. A. Pazmiño Betancourt, F. Vargas-Lara, F. W. Starr and J. F. Douglas, *J. Chem. Phys.*, 2019, **151**, 124705.

16 N. Jouault, J. F. Moll, D. Meng, K. Windsor, S. Ramcharan, C. Kearney and S. K. Kumar, *ACS Macro Lett.*, 2013, **2**, 371–374.

17 A. P. Holt, P. J. Griffin, V. Bocharova, A. L. Agapov, A. E. Imel, M. D. Dadmun, J. R. Sangoro and A. P. Sokolov, *Macromolecules*, 2014, **47**, 1837–1843.

18 S. Cheng, S. J. Xie, J. M. Y. Carrillo, B. Carroll, H. Martin, P. F. Cao, M. D. Dadmun, B. G. Sumpter, V. N. Novikov, K. S. Schweizer and A. P. Sokolov, *ACS Nano*, 2017, **11**, 752–759.

19 H. Zhang, P. Kalvapalle and J. F. Douglas, *Soft Matter*, 2010, **6**, 5944–5955.

20 F. W. Starr, J. F. Douglas, D. Meng and S. K. Kumar, *ACS Nano*, 2016, **10**, 10960–10965.

21 H. Emamy, S. K. Kumar and F. W. Starr, *Phys. Rev. Lett.*, 2018, **121**, 207801.

22 F. W. Starr and J. F. Douglas, *Phys. Rev. Lett.*, 2011, **106**, 1–4.

23 B. A. Pazmiño Betancourt, J. F. Douglas and F. W. Starr, *Soft Matter*, 2013, **9**, 241–254.

24 D. Fenistein and M. Van Hecke, *Nature*, 2003, **425**, 256.

25 H. Chen, Y. He, G. J. Shiflet and S. J. Poon, *Nature*, 1994, **367**, 541–543.

26 Q. Wei, D. Jia, K. T. Ramesh and E. Ma, *Appl. Phys. Lett.*, 2002, **81**, 1240–1242.

27 Y. Zhang and A. L. Greer, *Appl. Phys. Lett.*, 2006, **89**, 0–3.

28 A. L. Greer, Y. Q. Cheng and E. Ma, *Mater. Sci. Eng., R*, 2013, **74**, 71–132.

29 P. S. Steif, F. Spaepen and J. W. Hutchinson, *Acta Metall.*, 1982, **30**, 447–455.

30 M. L. Falk and J. S. Langer, *Phys. Rev. E: Stat. Phys., Plasmas, Fluids, Relat. Interdiscip. Top.*, 1998, **57**, 7192–7205.

31 J. S. Langer, *Phys. Rev. E: Stat. Phys., Plasmas, Fluids, Relat. Interdiscip. Top.*, 2004, **70**, 12.

32 M. L. Falk and J. S. Langer, *Annu. Rev. Condens. Matter Phys.*, 2011, **2**, 353–373.

33 F. Varnik, L. Bocquet, J. L. Barrat and L. Berthier, *Phys. Rev. Lett.*, 2003, **90**, 4.

34 Y. Shi and M. L. Falk, *Phys. Rev. B: Condens. Matter Mater. Phys.*, 2006, **73**, 1–10.

35 A. Shavit and R. A. Riggleman, *Phys. Chem. Chem. Phys.*, 2014, **16**, 10301–10309.

36 R. J. S. Ivancic and R. A. Riggleman, *Soft Matter*, 2019, **15**, 4548–4561.

37 E. D. Cubuk, S. S. Schoenholz, J. M. Rieser, B. D. Malone, J. Rottler, D. J. Durian, E. Kaxiras and A. J. Liu, *Phys. Rev. Lett.*, 2015, **114**, 1–5.

38 E. D. Cubuk, R. J. S. Ivancic, S. S. Schoenholz, D. J. Strickland, A. Basu, Z. S. Davidson, J. Fontaine, J. L. Hor, Y. R. Huang, Y. Jiang, N. C. Keim, K. D. Koshigan, J. A. Lefever, T. Liu, X. G. Ma, D. J. Magagnosc, E. Morrow, C. P. Ortiz, J. M. Rieser, A. Shavit, T. Still, Y. Xu, Y. Zhang, K. N. Nordstrom, P. E. Arratia, R. W. Carpick, D. J. Durian, Z. Fakhraai, D. J. Jerolmack, D. Lee, J. Li, R. Riggleman, K. T. Turner, A. G. Yodh, D. S. Gianola and A. J. Liu, *Science*, 2017, **358**, 1033–1037.

39 S. S. Schoenholz, E. D. Cubuk, D. M. Sussman, E. Kaxiras and A. J. Liu, *Nat. Phys.*, 2016, **12**, 469–472.

40 E. D. Cubuk, S. S. Schoenholz, E. Kaxiras and A. J. Liu, *J. Phys. Chem. B*, 2016, **120**, 6139–6146.

41 S. S. Schoenholz, E. D. Cubuk, E. Kaxiras and A. J. Liu, *Proc. Natl. Acad. Sci. U. S. A.*, 2017, **114**, 263–267.

42 F. W. Starr, T. B. Schrøder and S. C. Glotzer, *Phys. Rev. E: Stat. Phys., Plasmas, Fluids, Relat. Interdiscip. Top.*, 2001, **64**, 5.

43 T. Desai, P. Keblinski and S. K. Kumar, *J. Chem. Phys.*, 2005, **122**, 134910.

44 K. Kremer and G. S. Grest, *J. Chem. Phys.*, 1990, **92**, 5057–5086.

45 P. Z. Hanakata, B. A. P. Betancourt, J. F. Douglas and F. W. Starr, *J. Chem. Phys.*, 2015, **142**, 234907.

46 S. Plimpton, *J. Comput. Phys.*, 1995, **117**, 1–19.

47 W. Li, J. M. Rieser, A. J. Liu, D. J. Durian and J. Li, *Phys. Rev. E: Stat., Nonlinear, Soft Matter Phys.*, 2015, **91**, 1–13.

48 M. Harrington, A. J. Liu and D. J. Durian, *Phys. Rev. E*, 2019, **99**, 1–14.

49 R. Candelier, A. Widmer-Cooper, J. K. Kummerfeld, O. Dauchot, G. Biroli, P. Harrowell and D. R. Reichman, *Phys. Rev. Lett.*, 2010, **105**, 1–4.

50 A. Smessaert and J. Rottler, *Phys. Rev. E: Stat., Nonlinear, Soft Matter Phys.*, 2013, **88**, 1–11.

51 D. M. Sussman, S. S. Schoenholz, E. D. Cubuk and A. J. Liu, *Proc. Natl. Acad. Sci. U. S. A.*, 2017, **114**, 10601–10605.

52 A. Stukowski, *Modell. Simul. Mater. Sci. Eng.*, 2010, **18**, 015012.